Available online at www.sciencedirect.com
ScienceDirect
Journal of Power Sources 167 (2007) 430–441
JOURNAL OF POWER SOURCES
www.elsevier.com/locate/jpowsour

Non-destructive delamination detection in solid oxide fuel cells

J.I. Gazzarri *, O. Kesler

Department of Mechanical Engineering, University of British Columbia, 2054-6250 Applied Science Lane, Vancouver, BC V6T 1Z4, Canada

Received 19 January 2007; received in revised form 19 February 2007; accepted 19 February 2007
Available online 27 February 2007

Abstract

A finite element model has been developed to simulate the steady state and impedance behaviour of a single operating solid oxide fuel cell (SOFC). The model results suggest that electrode delamination can be detected minimally-invasively by using electrochemical impedance spectroscopy. The presence of cathode delamination causes changes in the cell impedance spectrum that are characteristic of this type of degradation mechanism. These changes include the simultaneous increase in both the series and polarization resistances, in proportion to the delaminated area. Parametric studies show the dependence of these changes on the extent of delamination, on the operating point, and on the kinetic characteristics of the fuel cell under study.

Keywords: Solid oxide fuel cell; Delamination; Impedance spectroscopy; Modeling; Degradation; Diagnostics

1. Introduction

Solid oxide fuel cells (SOFCs) are promising candidates to replace fossil fuel combustion for power generation. Not only is this type of fuel cell very efficient, but it is also flexible in terms of the many types of fuel that it can utilize. The SOFC has no moving parts, which would ease its maintenance requirements, and its high temperature of operation makes its exhaust heat usable in a turbine bottoming cycle, allowing overall efficiencies of approximately 80% to be achieved [1]. Despite these advantages, there are a number of still unresolved technical problems that prevent SOFCs from being commercially successful. These problems are related to the reliability, durability, and cost of the fuel cells. This work addresses a phenomenon that affects both the reliability and durability of the SOFC.

The high temperature of operation of the SOFC, essential to ensure adequate reaction kinetics and electrical conductivity of the electrolyte, poses important challenges on the cell materials. These materials need to undergo repeated thermal cycling from room temperature to operating temperature, and are cycled to even higher processing temperatures during manufacturing, with the consequent thermal stress generation due to differences in thermal expansion coefficients of adjacent cell layers. This load cycling may lead to degradation of the interfaces between layers, with eventual detachment occurring. This phenomenon is known as delamination, and it has been documented as an important mechanical degradation mechanism in SOFCs [2–4].

Upon the occurrence of delamination, the cell performance deteriorates because the open gap, perpendicular to the main current path, constitutes an insulating barrier to charge conduction, and destroys electrochemical reaction sites. These processes result in the under-utilization of the fuel cell's effective area. Under standard degradation test conditions, the cell delivers a constant current as its voltage is monitored over time. Upon the occurrence of delamination, the current density increases over the remaining intact cell area in order to maintain the constant current being drawn from the cell, which produces a drop in the electric potential. Other degradation mechanisms also cause a reduction of the delivered potential in the aforementioned degradation test conditions. From the maintenance standpoint, however, it is important to recognize and distinguish between different degradation mechanisms because, in general, each of them requires a different corrective action. Disassembling the fuel cell stack to diagnose it is an option, but it is undesirable because it requires taking the stack out of service, and introduces additional degradation caused by the extra thermal cycle. Because some types of degradation can be reversed by modifying the operating conditions (e.g. sulfur poisoning [5]), a diagnostic technique that can distinguish between different modes of degradation in a minimally-invasive

* Corresponding author. Tel.: +1 604 822 4745; fax: +1 604 822 2403.
E-mail address: javier@mech.ubc.ca (J.I. Gazzarri).

0378-7753/$ – see front matter © 2007 Elsevier B.V. All rights reserved.
doi:10.1016/j.jpowsour.2007.02.042

manner while the stack is still in operation is preferable to disassembly and inspection of the stack for diagnosis.

There are several SOFC applications or operating conditions in which delamination is particularly likely to occur, and where a minimally invasive diagnostic tool to assess mechanical damage could be very useful. Auxiliary power units, also known as APUs, are power generators used for peripheral devices on vehicles such as trucks and motor-homes, in order to avoid extended periods of combustion engine idling. In this application, repeated thermal cycling is unavoidable, and mechanical damage is prone to occur due to thermal expansion coefficient mismatch of SOFC components.

A second example is redox instability of Ni-YSZ SOFC anodes. Nickel is the most popular catalyst used in SOFC anodes. However, it easily oxidises to NiO if the oxygen partial pressure inside the anode chamber is not kept sufficiently low. This is a common scenario during emergency power shutdowns in which fuel is no longer supplied. Further examples of causes of high P_{O2} in the anode are air leaks due to seal failure, periodic air treatment of the anode to prevent incipient carbon deposition, or very high fuel utilization conditions, resulting in high concentrations of steam at the anode exhaust. This oxidation of Ni produces a volume expansion of the anode functional layer that can lead to mechanical damage, including delamination of the anode from the electrolyte. Although oxidation of nickel in the anode is a reversible phenomenon (the NiO can be re-reduced back to nickel on re-introduction of H_2 to the anode), it can lead to irreversible cell damage.

Both thermal cycling of APUs and anode redox cycling are examples of the potential benefits of having a minimally invasive diagnostic technique that can be used to detect delamination in situ, thus, justifying the need to disassemble the stack to replace or bypass the affected cell or cells. This work describes a finite element model of a single solid oxide fuel cell, to be used as part of a diagnostic technique for identifying delamination non-invasively in an operating SOFC. The model can be used to predict both DC electrical performance and AC impedance spectra of a working cell as a function of geometry, materials, and operating conditions.

The idea of identifying mechanical damage in materials using impedance spectroscopy has been reported in the literature since the early 1990s. Working with structural ceramics, Kleitz et al. [6,7] showed a change in the overall resistivity and permittivity of an object as a function of internal crack growth. They attributed this behaviour to the creation of blocking interfaces that acted as a hindrance to ion movement. Tiefenbach [8–10] found a new relaxation time in the impedance spectrum of an 8 mol% yttria-stabilized zirconia (8YSZ) sample caused by the growth of a crack. They attributed this result to the different permittivity of the air contained in the gap compared to the permittivity of the surrounding material. The aim of their work was to detect the presence of phase transformation induced microcracks in the bulk of a ceramic. Fleig and Maier [11] found that imperfect contact of silver electrodes on CaF_2 gives rise to a new semicircle in the impedance spectrum. They proposed an equivalent circuit to describe the influence of the gap created by the imperfect contact on the impedance behaviour of the ceramic.

These studies showed the potential of impedance spectroscopy for the detection of mechanical degradation in ceramics. However, the concept has not previously been applied to ceramic fuel cells, to the authors' knowledge. In SOFCs, the fuel cell internal processes have their own impedance signatures superimposed on the characteristic impedance behaviour of the cell materials, whereas in the inert ceramics previously studied, the impedance spectrum corresponds to the ceramic material electrical behaviour only. The superposition of the impedance features associated with mechanical degradation on the cells own impedance features poses additional challenges in terms of the proposed method resolution. In addition, the operating temperatures of the SOFCs are much higher than the temperatures studied in the previous contributions (200–400 °C), thus complicating the identification of some defect-related signatures at frequencies that are experimentally accessible, as will be explained in later sections.

In this paper, we present a finite element model of the impedance behaviour of a single cell SOFC, and we present modeling results for the baseline case of an intact cell and for cases in which a delamination is present. Parametric studies show trends in the impedance spectrum with variations in delaminated area and in the electrode kinetics of the fuel cell.

2. Numerical model

The geometry of a planar solid oxide fuel cell stack consists of multiple anode-electrolyte-cathode assemblies, separated by interconnect plates that provide series electrical connection and channels for reactant delivery. The model described in the present work is restricted to a single cell and does not include the interconnect plates. The geometry of the model is further restricted to two dimensions, where we consider both rectangular and polar axisymmetric coordinates. Rectangular coordinates are used to model commercially available square planar cells, and allow the introduction of the model equations in the simplest possible terms, while the equations in axisymmetric coordinates can be used to model button cells commonly used in laboratory-scale experimental work.

2.1. Cartesian coordinates

Fig. 1 shows a schematic of the modeled geometry in Cartesian coordinates. The large aspect ratio required to represent the geometry of an SOFC requires a careful meshing procedure so

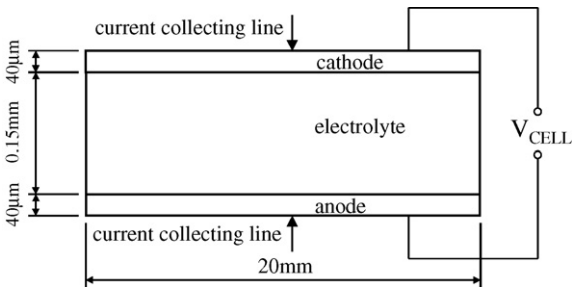

Fig. 1. Schematic of the modeled 2-D SOFC geometry.

that the finite element dimensions provide both adequate resolution and acceptable computing times. At the electrodes, the mesh was structured so that the element size decreases towards the interface with the electrolyte. In the direction perpendicular to the main current density vector, the mesh can be much coarser. The optimal mesh was checked against an overly refined mesh with which the simulation was run for an extended period of time.

The simulated SOFC is electrolyte-supported, using 8 mol% yttria-stabilized zirconia (8YSZ) for the electrolyte, a 50% vol lanthanum strontium manganite (LSM)/50% vol YSZ composite for the cathode, and a 40% vol Ni/60% vol YSZ composite for the anode, with both electrodes having 40% porosity. Electrochemical data were taken from the literature. As a first approximation, the model neglects any reactant concentration gradients, corresponding to very low fuel utilization, as well as any concentration polarization. The system is also approximated as isothermal. These assumptions are valid for small electrolyte-supported cells with thin electrodes and high fuel and oxidant stoichiometries, as in typical experimental conditions used for testing single button-type cells. These initial assumptions can be further refined for application of the model to an operating stack.

The simulation consists of the solution of the charge conservation equations for both direct and for alternating current. The equations are solved for ions and for electrons in the cathode and anode, and for ions only in the electrolyte. The porous electrodes are modeled as continuum materials with an effective electronic and ionic conductivity at every point corresponding to their averaged porous composite properties, and with a constant concentration of reactant throughout their thickness, as described by Newman and Tobias [12]. The electrochemical reactions occur at the electrodes over a finite distance from the electrode/electrolyte interface that depends on the reaction rate and the effective ionic conductivity of the electrodes. The modeled reactants are hydrogen and air, and the electrochemical reactions exhibit a Butler–Volmer dependence of current on overpotential. The four dependent variables are the ionic and electronic potentials, both for direct and for alternating current.

The general form of the charge balance equations is:

$$\nabla \cdot i = Si_{\mathrm{F}}(\eta) + SC_{\mathrm{dl}}\frac{\partial \eta}{\partial t} \tag{1}$$

where i is the ionic or electronic current density vector ($\mathrm{A\,m^{-2}}$), S is the electrochemically active surface area of the medium per unit volume ($\mathrm{m^{-1}}$), i_{F} is the Faradaic current density ($\mathrm{A\,m^{-2}}$), η is the local overpotential (V), C_{dl} is the double layer capacitance associated with the interface between the ionic and electronic conducting phases ($\mathrm{F\,m^{-2}}$), and t is the time (s). The overpotential is defined as the difference between the potentials of the electronic (Φ_{ELE}) and ionic (Φ_{ION}) phases with respect to equilibrium potential (Φ_{REF}):

$$\eta = \Phi_{\mathrm{ELE}} - \Phi_{\mathrm{ION}} - \Phi_{\mathrm{REF}} \tag{2}$$

Eq. (1) states that the flux of charge from within an elementary volume must balance the volumetric production or consumption of charge, plus the charge or discharge of the interfacial double layer. Ohm's law relates current density and potential:

$$i = -k\nabla\Phi \tag{3}$$

where k is the effective (i.e. it considers porosity and tortuosity) conductivity for the species (ions or electrons) in the medium ($\mathrm{Ohm^{-1}\,m^{-1}}$), and Φ is the electric (ionic or electronic) potential (V). Substituting the current density in Eq. (1) by the expression given by (3) yields:

$$-\nabla \cdot (k\nabla\Phi) = Si_{\mathrm{F}}(\eta) + SC_{\mathrm{dl}}\frac{\partial \eta}{\partial t} \tag{4}$$

If the effective conductivity k is independent of the spatial coordinates, the divergence term becomes the Laplacian of the potential: $-k\nabla^2\Phi$. This assumption holds hereafter in this work.

A further simplification of Eq. (4) is possible in the DC case, for which the time derivative vanishes, yielding:

$$-k\nabla^2\Phi = Si_{\mathrm{F}}(\eta) \tag{5}$$

No double layer charging occurs in this case.

The Faradaic current density is associated with the charge transfer that occurs when a species moves from one medium to another in an electrochemical reaction. A function of the local overpotential, its magnitude reflects the electrochemical activity at a point in the electrode. In this work, we assume a Butler–Volmer relationship between overpotential and Faradaic current density. For example, the Faradaic ionic current generated in the DC cathodic reaction is given by:

$$i_{\mathrm{F,ION,CAT}}(\eta) = i_{0,\mathrm{CAT}}\left[\exp\left(\frac{\alpha_{\mathrm{CAT,ANO}}F}{RT}\eta_{\mathrm{CAT}}\right) - \exp\left(-\frac{\alpha_{\mathrm{CAT,CAT}}F}{RT}\eta_{\mathrm{CAT}}\right)\right] \tag{6}$$

where $i_{0,\mathrm{CAT}}$ is the cathodic exchange current density ($\mathrm{A\,m^{-2}}$), α_{ij} is the charge transfer coefficient for the reaction with the first subindex indicating the electrode and the second subindex indicating the anodic or cathodic direction, F is the Faraday's constant ($\mathrm{A\,s\,mol^{-1}}$), R is the univeral gas constant ($\mathrm{J\,mol^{-1}\,K^{-1}}$), and T is the absolute temperature (K). The reference potentials are those corresponding to open circuit against a reference electrode. As will be discussed later, obtaining realistic values for these parameters constitutes an important challenge within the field of fuel cell modeling.

Charge conservation must hold at all locations within the electrode. Mathematically, this requires that the sum of the ionic and electronic current fluxes from each volume element cancel out:

$$\nabla \cdot i_{\mathrm{ION}} + \nabla \cdot i_{\mathrm{ELE}} = 0 \tag{7}$$

Therefore, the Faradaic current density corresponding to the electronic charge balance given by Eq. (5) is identical in magnitude to that of Eq. (6), but with opposite sign:

$$i_{\mathrm{F,ELE,CAT}}(\eta) = -i_{0,\mathrm{CAT}}\left[\exp\left(\frac{\alpha_{\mathrm{CAT,ANO}}F}{RT}\eta_{\mathrm{CAT}}\right) - \exp\left(-\frac{\alpha_{\mathrm{CAT,CAT}}F}{RT}\eta_{\mathrm{CAT}}\right)\right] \tag{8}$$

Analogous expressions apply to the anode side of the cell, with the appropriate anodic kinetic terms replacing those for the cathode. The ionic and electronic Faradaic current density for the anode is given in Eqs. (9) and (10), respectively.

$$i_{\mathrm{F,ION,ANO}}(\eta) = i_{0,\mathrm{ANO}}\left[\exp\left(\frac{\alpha_{\mathrm{ANO,ANO}}F}{RT}\eta_{\mathrm{ANO}}\right) - \exp\left(-\frac{\alpha_{\mathrm{ANO,CAT}}F}{RT}\eta_{\mathrm{ANO}}\right)\right] \tag{9}$$

$$i_{\mathrm{F,ELE,ANO}}(\eta) = -i_{0,\mathrm{ANO}}\left[\exp\left(\frac{\alpha_{\mathrm{ANO,ANO}}F}{RT}\eta_{\mathrm{ANO}}\right) - \exp\left(-\frac{\alpha_{\mathrm{ANO,CAT}}F}{RT}\eta_{\mathrm{ANO}}\right)\right] \tag{10}$$

Using the appropriate Faradaic source terms from Eqs. (6), (8)–(10) in the DC charge balance of Eq. (5), the set of DC equations valid in the electrodes is:

$$\begin{aligned}
-k_{\mathrm{ION,CAT}}\nabla^2\Phi_{\mathrm{ION}} &= S_{\mathrm{CAT}}i_{0,\mathrm{CAT}}\left[\exp\left(\frac{\alpha_{\mathrm{CAT,ANO}}F}{RT}\eta_{\mathrm{CAT}}\right) - \exp\left(-\frac{\alpha_{\mathrm{CAT,CAT}}F}{RT}\eta_{\mathrm{CAT}}\right)\right]\\
-k_{\mathrm{ELE,CAT}}\nabla^2\Phi_{\mathrm{ELE}} &= -S_{\mathrm{CAT}}i_{0,\mathrm{CAT}}\left[\exp\left(\frac{\alpha_{\mathrm{CAT,ANO}}F}{RT}\eta_{\mathrm{CAT}}\right) - \exp\left(-\frac{\alpha_{\mathrm{CAT,CAT}}F}{RT}\eta_{\mathrm{CAT}}\right)\right]\\
-k_{\mathrm{ION,ANO}}\nabla^2\Phi_{\mathrm{ION}} &= S_{\mathrm{ANO}}i_{0,\mathrm{ANO}}\left[\exp\left(\frac{\alpha_{\mathrm{ANO,ANO}}F}{RT}\eta_{\mathrm{ANO}}\right) - \exp\left(-\frac{\alpha_{\mathrm{ANO,CAT}}F}{RT}\eta_{\mathrm{ANO}}\right)\right]\\
-k_{\mathrm{ELE,ANO}}\nabla^2\Phi_{\mathrm{ELE}} &= -S_{\mathrm{ANO}}i_{0,\mathrm{ANO}}\left[\exp\left(\frac{\alpha_{\mathrm{ANO,ANO}}F}{RT}\eta_{\mathrm{ANO}}\right) - \exp\left(-\frac{\alpha_{\mathrm{ANO,CAT}}F}{RT}\eta_{\mathrm{ANO}}\right)\right]
\end{aligned} \tag{11}$$

In these expressions, $\eta_{\mathrm{CAT}} = \Phi_{\mathrm{ELE}} - \Phi_{\mathrm{ION}} - \Phi_{\mathrm{REF,CAT}}$, the cathodic overpotential, is a negative scalar and $\eta_{\mathrm{ANO}} = \Phi_{\mathrm{ELE}} - \Phi_{\mathrm{ION}} - \Phi_{\mathrm{REF,ANO}}$, the anodic overpotential, is a positive scalar.

The only DC equation for the electrolyte corresponds to the ionic current balance, and the absence of electrochemical reactions in this domain implies that the Faradaic source term is equal to zero:

$$\nabla^2\Phi_{\mathrm{ION}} = 0 \tag{12}$$

Physically, this equation implies that across the electrolyte thickness, the ionic potential is linear, and that the ionic current density is constant.

These DC Eqs. (11) and (12) are solved with a finite element solver (Comsol Multiphysics, Comsol AB), using boundary conditions of the Dirichlet type for the electronic potentials at the current collectors:

$$\begin{aligned}
\Phi|_{\text{cathode current collector}} &= V_{\mathrm{CELL}}\\
\Phi|_{\text{anoode current collector}} &= 0\ V
\end{aligned} \tag{13}$$

Here V_{CELL} is the operating voltage of the cell. The electronic potential at all other boundaries, and all ionic potentials, have Neumann (insulation) boundary conditions:

$$\frac{\partial\Phi}{\partial n} = 0 \tag{14}$$

The AC charge conservation equations derive from assuming linearity in the current response to a voltage perturbation, which is a fundamental supposition behind the study of impedance spectra. This assumption implies that the current response to a small sinusoidal voltage perturbation is also sinusoidal and of the same frequency. As an example, we consider the application of the charge balance in Eq. (4) to the ionic current in the cathode:

$$\begin{aligned}
-k_{\mathrm{ION,CAT}}\nabla^2\Phi_{\mathrm{ION}} = S_{\mathrm{CAT}}C_{\mathrm{dl,CAT}}\frac{\partial\eta_{\mathrm{CAT}}}{\partial t} + S_{\mathrm{CAT}}i_{0,\mathrm{CAT}}\\
\times\left[\exp\left(\frac{\alpha_{\mathrm{CAT,ANO}}F}{RT}\eta_{\mathrm{CAT}}\right) - \exp\left(-\frac{\alpha_{\mathrm{CAT,CAT}}F}{RT}\eta_{\mathrm{CAT}}\right)\right]
\end{aligned} \tag{15}$$

Now, both the ionic and electronic potentials have a DC component (given by the operating point) and an AC component (given by the perturbation magnitude), where j is the square root of -1:

$$\begin{aligned}
\Phi_{\mathrm{ELE}} &= \Phi_{\mathrm{ELE}}^{\mathrm{DC}} + \Phi_{\mathrm{ELE}}^{\mathrm{AC}}\,e^{j\omega t}\\
\Phi_{\mathrm{ION}} &= \Phi_{\mathrm{ION}}^{\mathrm{DC}} + \Phi_{\mathrm{ION}}^{\mathrm{AC}}e^{j\omega t}
\end{aligned} \tag{16}$$

Substituting the expressions in Eq. (16) into Eq. (15), we obtain:

$$\begin{aligned}
&-k_{\mathrm{ION,CAT}}\nabla^2\Phi_{\mathrm{ION}}^{\mathrm{DC}} - e^{j\omega t}k_{\mathrm{ION,CAT}}\nabla^2\Phi_{\mathrm{ION}}^{\mathrm{AC}}\\
&= S_{\mathrm{CAT}}C_{\mathrm{dl,CAT}}\frac{\partial}{\partial t}(\Phi_{\mathrm{ELE}}^{\mathrm{AC}}e^{j\omega t} - \Phi_{\mathrm{ION}}^{\mathrm{AC}}e^{j\omega t}) + S_{\mathrm{CAT}}i_{0,\mathrm{CAT}}\\
&\quad\times\exp\left(\frac{\alpha_{\mathrm{CAT,ANO}}F}{RT}(\Phi_{\mathrm{ELE}}^{\mathrm{AC}} - \Phi_{\mathrm{ION}}^{\mathrm{AC}})e^{j\omega t}\right)\\
&\quad\times\exp\left(\frac{\alpha_{\mathrm{CAT,ANO}}F}{RT}\eta_{\mathrm{CAT}}^{\mathrm{DC}}\right) - S_{\mathrm{CAT}}i_{0,\mathrm{CAT}}\\
&\quad\times\exp\left(-\frac{\alpha_{\mathrm{CAT,CAT}}F}{RT}(\Phi_{\mathrm{ELE}}^{\mathrm{AC}} - \Phi_{\mathrm{ION}}^{\mathrm{AC}})\,e^{j\omega t}\right)\\
&\quad\times\exp\left(-\frac{\alpha_{\mathrm{CAT,CAT}}F}{RT}\eta_{\mathrm{CAT}}^{\mathrm{DC}}\right)
\end{aligned} \tag{17}$$

The Faradaic source terms now have the time-dependent harmonic factor inside an exponential term. On account of the

small size of the perturbation, each exponential function can be expanded to its first order Taylor series around

$\Phi_{\mathrm{ELE}}^{\mathrm{AC}} - \Phi_{\mathrm{ION}}^{\mathrm{AC}} = 0$

This step leads to the linearizations.

$$\exp\left(\frac{\alpha_{\mathrm{CAT,ANO}}F}{RT}(\Phi_{\mathrm{ELE}}^{\mathrm{AC}} - \Phi_{\mathrm{ION}}^{\mathrm{AC}})e^{j\omega t}\right) \approx 1 + \frac{\alpha_{\mathrm{CAT,ANO}}F}{RT}(\Phi_{\mathrm{ELE}}^{\mathrm{AC}} - \Phi_{\mathrm{ION}}^{\mathrm{AC}})e^{j\omega t} \tag{18}$$

and

$$\exp\left(-\frac{\alpha_{\mathrm{CAT,CAT}}F}{RT}(\Phi_{\mathrm{ELE}}^{\mathrm{AC}} - \Phi_{\mathrm{ION}}^{\mathrm{AC}})\, e^{j\omega t}\right) \approx 1 - \frac{\alpha_{\mathrm{CAT,CAT}}F}{RT}(\Phi_{\mathrm{ELE}}^{\mathrm{AC}} - \Phi_{\mathrm{ION}}^{\mathrm{AC}})e^{j\omega t} \tag{19}$$

Substituting these expressions in Eq. (17), we obtain:

$$\begin{aligned}
&-k_{\mathrm{ION,CAT}}\nabla^2\Phi_{\mathrm{ION}}^{\mathrm{DC}} - e^{j\omega t}k_{\mathrm{ION,CAT}}\nabla^2\Phi_{\mathrm{ION}}^{\mathrm{AC}} \\
&\quad = S_{\mathrm{CAT}}C_{\mathrm{dl,CAT}}j\omega\, e^{j\omega t}(\Phi_{\mathrm{ELE}}^{\mathrm{AC}} - \Phi_{\mathrm{ION}}^{\mathrm{AC}}) + S_{\mathrm{CAT}}i_{0,\mathrm{CAT}}\left[\exp\left(\frac{\alpha_{\mathrm{CAT,ANO}}F}{RT}\eta_{\mathrm{CAT}}^{\mathrm{DC}}\right) - \exp\left(-\frac{\alpha_{\mathrm{CAT,CAT}}F}{RT}\eta_{\mathrm{CAT}}^{\mathrm{DC}}\right)\right] \\
&\quad + S_{\mathrm{CAT}}i_{0,\mathrm{CAT}}\frac{\alpha_{\mathrm{CAT,ANO}}F}{RT}(\Phi_{\mathrm{ELE}}^{\mathrm{AC}} - \Phi_{\mathrm{ION}}^{\mathrm{AC}})e^{j\omega t}\exp\left(\frac{\alpha_{\mathrm{CAT,ANO}}F}{RT}\eta_{\mathrm{CAT}}^{\mathrm{DC}}\right) + S_{\mathrm{CAT}}i_{0,\mathrm{CAT}}\frac{\alpha_{\mathrm{CAT,CAT}}F}{RT}(\Phi_{\mathrm{ELE}}^{\mathrm{AC}} - \Phi_{\mathrm{ION}}^{\mathrm{AC}})e^{j\omega t} \\
&\quad \times\exp\left(-\frac{\alpha_{\mathrm{CAT,CAT}}F}{RT}\eta_{\mathrm{CAT}}^{\mathrm{DC}}\right)
\end{aligned} \tag{20}$$

The terms in this expression that do not contain the harmonic $\exp(j\omega t)$ factor constitute the DC Eq. (11) already described, and they cancel out of the expression. Eliminating the common factor $\exp(j\omega t)$ from the rest of the terms, the following expression is obtained:

$$\begin{aligned}
-k_{\mathrm{ION,CAT}}\nabla^2\Phi_{\mathrm{ION}}^{\mathrm{AC}} &= S_{\mathrm{CAT}}C_{\mathrm{dl,CAT}}j\omega(\Phi_{\mathrm{ELE}}^{\mathrm{AC}} - \Phi_{\mathrm{ION}}^{\mathrm{AC}}) + S_{\mathrm{CAT}}i_{0,\mathrm{CAT}}\frac{\alpha_{\mathrm{CAT,ANO}}F}{RT}(\Phi_{\mathrm{ELE}}^{\mathrm{AC}} - \Phi_{\mathrm{ION}}^{\mathrm{AC}}) \\
&\quad\times\exp\left(\frac{\alpha_{\mathrm{CAT,ANO}}F}{RT}\eta_{\mathrm{CAT}}^{\mathrm{DC}}\right) + S_{\mathrm{CAT}}i_{0,\mathrm{CAT}}\frac{\alpha_{\mathrm{CAT,CAT}}F}{RT}(\Phi_{\mathrm{ELE}}^{\mathrm{AC}} - \Phi_{\mathrm{ION}}^{\mathrm{AC}})\exp\left(-\frac{\alpha_{\mathrm{CAT,CAT}}F}{RT}\eta_{\mathrm{CAT}}^{\mathrm{DC}}\right)
\end{aligned} \tag{21}$$

This equation is solved for the desired range of frequencies in the different domains. An important point here is that $\eta_{\mathrm{CAT}}^{\mathrm{DC}}$, the DC overpotential, is already known from the solution to the DC equations. Therefore there is no need to solve all the DC and AC equations simultaneously. Instead, the DC case is solved first, and then the AC case is solved, making use of the DC solution. Of course, this statement also applies to the anode case. A summary of the AC equations for cathode ionic, cathode electronic, anode ionic, anode electronic, and electrolyte ionic current, respectively, is given as follows, where $\eta^{\mathrm{AC}} = \Phi_{\mathrm{ELE}}^{\mathrm{AC}} - \Phi_{\mathrm{ION}}^{\mathrm{AC}}$:

$$\begin{aligned}
&-k_{\mathrm{ION,CAT}}\nabla^2\Phi_{\mathrm{ION}}^{\mathrm{AC}} = S_{\mathrm{CAT}}C_{\mathrm{dl,CAT}}j\omega\eta^{\mathrm{AC}} + S_{\mathrm{CAT}}i_{0,\mathrm{CAT}}\left(\frac{\alpha_{\mathrm{CAT,ANO}}F}{RT}\eta^{\mathrm{AC}}\exp\left(\frac{\alpha_{\mathrm{CAT,ANO}}F}{RT}\eta_{\mathrm{CAT}}^{\mathrm{DC}}\right) + \frac{\alpha_{\mathrm{CAT,CAT}}F}{RT}\eta^{\mathrm{AC}}\exp\left(-\frac{\alpha_{\mathrm{CAT,CAT}}F}{RT}\eta_{\mathrm{CAT}}^{\mathrm{DC}}\right)\right) \\
&-k_{\mathrm{ELE,CAT}}\nabla^2\Phi_{\mathrm{ELE}}^{\mathrm{AC}} = -S_{\mathrm{CAT}}C_{\mathrm{dl,CAT}}j\omega\eta^{\mathrm{AC}} - S_{\mathrm{CAT}}i_{0,\mathrm{CAT}}\left(\frac{\alpha_{\mathrm{CAT,ANO}}F}{RT}\eta^{\mathrm{AC}}\exp\left(\frac{\alpha_{\mathrm{CAT,ANO}}F}{RT}\eta_{\mathrm{CAT}}^{\mathrm{DC}}\right) + \frac{\alpha_{\mathrm{CAT,CAT}}F}{RT}\eta^{\mathrm{AC}}\exp\left(-\frac{\alpha_{\mathrm{CAT,CAT}}F}{RT}\eta_{\mathrm{CAT}}^{\mathrm{DC}}\right)\right) \\
&-k_{\mathrm{ION,ANO}}\nabla^2\Phi_{\mathrm{ION}}^{\mathrm{AC}} = S_{\mathrm{ANO}}C_{\mathrm{dl,ANO}}j\omega\eta^{\mathrm{AC}} + {}_{\mathrm{ANO}}i_{0,\mathrm{ANO}}\left(\frac{\alpha_{\mathrm{ANO,ANO}}F}{RT}\eta^{\mathrm{AC}}\exp\left(\frac{\alpha_{\mathrm{ANO,ANO}}F}{RT}\eta_{\mathrm{ANO}}^{\mathrm{DC}}\right) + \frac{\alpha_{\mathrm{ANO,CAT}}F}{RT}\eta^{\mathrm{AC}}\exp\left(-\frac{\alpha_{\mathrm{ANO,CAT}}F}{RT}\eta_{\mathrm{ANO}}^{\mathrm{DC}}\right)\right) \\
&-k_{\mathrm{ELE,ANO}}\nabla^2\Phi_{\mathrm{ION}}^{\mathrm{AC}} = -S_{\mathrm{ANO}}C_{\mathrm{dl,ANO}}j\omega\eta^{\mathrm{AC}} - S_{\mathrm{ANO}}i_{0,\mathrm{ANO}}\left(\frac{\alpha_{\mathrm{ANO,ANO}}F}{RT}\eta^{\mathrm{AC}}\exp\left(\frac{\alpha_{\mathrm{ANO,ANO}}F}{RT}\eta_{\mathrm{ANO}}^{\mathrm{DC}}\right) + \frac{\alpha_{\mathrm{ANO,CAT}}F}{RT}\eta^{\mathrm{AC}}\exp\left(-\frac{\alpha_{\mathrm{ANO,CAT}}F}{RT}\eta_{\mathrm{ANO}}^{\mathrm{DC}}\right)\right) \\
&-k_{\mathrm{ION,ELY}}\nabla^2\Phi_{\mathrm{ION}}^{\mathrm{AC}} = 0
\end{aligned} \tag{22}$$

The boundary conditions for the AC equations are:

$$\begin{aligned}
\Phi^{\mathrm{AC}}|_{\text{cathode current collector}} &= -\Delta\Phi_0^{\mathrm{AC}} \\
\Phi^{\mathrm{AC}}|_{\text{anode current collector}} &= +\Delta\Phi_0^{\mathrm{AC}}
\end{aligned} \tag{23}$$

where $\Delta\Phi_0^{\mathrm{AC}}$ is the perturbation amplitude. Again, Neumann (insulation) boundary conditions apply everywhere else for the electronic potential, and everywhere for the ionic potentials.

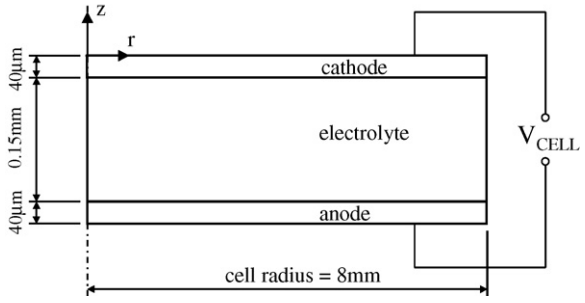

Fig. 2. Axisymmetric geometry of a single SOFC.

2.2. Axisymmetric coordinates

The geometry of a circular button cell used for laboratory-scale experimental testing makes cylindrical coordinates a convenient choice for a 2-D axisymmetric simulation. This case corresponds to the geometry in Fig. 2, with the same layer thicknesses as in the Cartesian coordinate system. In terms of the model equations, the only modification needed is in the expression of the divergence, where

$$k\nabla^2\Phi = k\left(\frac{1}{r}\frac{\partial}{\partial r}\left(r\frac{\partial\Phi}{\partial r}\right)+\frac{\partial^2\Phi}{\partial z^2}\right) \tag{24}$$

The numerical simulations presented in this work were also performed using Cartesian coordinates. The conclusions presented in this work are valid for both the Cartesian and the axisymmetric geometries.

2.3. Calculation of the impedance

Upon calculation of the four unknown potentials, the current densities (in $\mathrm{A\,m^{-2}}$) are calculated as the negative gradient of the potential times the corresponding conductivity:

$$\begin{aligned} i_{\mathrm{ION}}^{\mathrm{DC}} &= -k_{\mathrm{ION}}\nabla\Phi_{\mathrm{ION}}^{\mathrm{DC}} \\ i_{\mathrm{ELE}}^{\mathrm{DC}} &= -k_{\mathrm{ELE}}\nabla\Phi_{\mathrm{ELE}}^{\mathrm{DC}} \\ i_{\mathrm{ION}}^{\mathrm{AC}} &= -k_{\mathrm{ION}}\nabla\Phi_{\mathrm{ION}}^{\mathrm{AC}} \\ i_{\mathrm{ELE}}^{\mathrm{AC}} &= -k_{\mathrm{ELE}}\nabla\Phi_{\mathrm{ELE}}^{\mathrm{AC}} \end{aligned} \tag{25}$$

The impedance is the ratio between the applied voltage perturbation magnitude and the AC current density computed at any of the current collectors.

$$Z(\omega) = \frac{2\Delta\Phi^{\mathrm{AC}}}{i_{\mathrm{ELE}}^{\mathrm{AC}}(\omega)\big|_{\text{current collector}}} \tag{26}$$

The AC current density is a complex number, and in general it has a phase shift with respect to the applied potential. As a consequence, the impedance is also complex-valued. Traditionally, the impedance is presented in Cartesian plots of its negative imaginary part as a function of its real part (Nyquist plot), or of its magnitude and phase shift as a function of the logarithm of the frequency (Bode plots). The Nyquist plot of the impedance spectrum of SOFCs usually exhibits one or more flattened semicircles and/or straight lines, due to the capacitive behaviour of the electrochemical processes involved. The relative position of these semicircles, their size, the apex frequencies, and the values of their intercepts with the real axis yield important information on the different processes within the cell.

2.4. Input parameters

To obtain input values for the model, we utilized data published in the literature. However, there is considerable disagreement in the literature regarding the charge transfer coefficients, the nature of the rate-limiting step for the electrode half-cell reactions, and the exchange current densities. Moreover, the active surface area can be modified substantially through control of the microstructure by use of different manufacturing techniques. Despite this variability from cell to cell, the model can be used to predict the change in the impedance spectrum for a specific operating SOFC when the kinetic and microstructural properties are known for that cell. Effective conductivity of the electrodes was calculated according to $k^{\mathrm{eff}} = k^{\mathrm{bulk}}x(1-\varepsilon)/\tau$ where x is the volumetric fraction of conductive material with conductivity k^{bulk} in the electrode, ε is the porosity volume fraction, and τ is the tortuosity factor [13]. This expression is valid for both ionic and electronic conductivities. A value of 3 was used for the tortuosity [14].

The cathodic reaction electrochemical parameters result from fitting the model to symmetric cathode experiments. For a given set of charge transfer coefficients [20], $S_{\mathrm{CAT}}\ i_{0,\mathrm{CAT}}$ is calculated so that the cathodic polarization resistance calculated by the model matches the experiment. Then, the double layer capacitance is calculated so as to reproduce the measured apex frequency.

In the case of the anode, we could not find a complete data set at the desired temperature, so $S_{\mathrm{ANO}}\ i_{0,\mathrm{ANO}}$ was estimated as equal to $S_{\mathrm{CAT}}\ i_{0,\mathrm{CAT}}$. The empirical observation that both polarization resistances are of the same order of magnitude [22] justifies this approximation for the use of H_2 as a simulated reactant. For direct oxidation of hydrocarbons at the anode, further adjustment to the kinetic values based on experimental data for hydrocarbons would be required. Large anodic charge transfer coefficients [19] yield a lower polarization resistance for the anode under operating loads, compared to that of the cathode. The method proposed in the present work for diagnosis of degradation is based on detecting changes in the impedance spectrum compared to that of an intact cell. These changes are not affected by the estimation of the electrochemical parameters, as will be shown later. The data used in the model are listed in Table 1.

2.5. Comparison with a simplified experiment

In order to assess the model's ability to represent experimental data, we measured the impedance spectrum of an in-house made symmetric cathode cell and fitted our model to it. The symmetric cell is a simple configuration that behaves similarly to a working cell near the equilibrium potential. The experimental cell consisted of a pressed and sintered YSZ (Inframat) pellet to which identical cathodes were screen printed on each side. The cathodes were LSM (50% vol)–YSZ (50% vol) composites, with approximately 40% porosity, achieved using carbon black as

Table 1
Input parameters used in the model for calculation of the impedance behaviour of the intact cell

Property	Symbol	Value	Units	References
Operating point	V	0.7	V	
Open circuit potential	OCV	1	V	[1]
Volumetric anode exchange current density	$S_{ano}\ i_{0,ANO}$	2.2×10^7	Am^{-3}	[15]
Volumetric cathode exchange current density	$S_{cat}\ i_{0,CAT}$	2.2×10^7	Am^{-3}	[16–18]
Double layer capacitance, anode	$C_{dl,ANO}$	0.4	Fm^{-2}	[1]
Double layer capacitance, cathode	$C_{dl,CAT}$	90	Fm^{-2}	[16–18]
Electrolyte ionic conductivity	$k_{ION,ELY}$	4.1	Sm^{-1}	[1]
Effective anode ionic conductivity	$k_{ION,ANO}$	0.29	Sm^{-1}	[13]
Effective cathode ionic conductivity	$k_{ION,CAT}$	0.24	Sm^{-1}	[13]
Effective anode electronic conductivity	$k_{ELE,ANO}$	4.8×10^3	Sm^{-1}	[13]
Effective cathode electronic conductivity	$k_{ELE,CAT}$	1.6×10^3	Sm^{-1}	[13]
Temperature	T	850	°C	
Peak to peak perturbation voltage	$\Delta\Phi_0{}^{AC}$	20	mV	
Charge transfer coefficients, anode	$\alpha_{ANO,\ ANO}$; $\alpha_{ANO,\ CAT}$	2; 1		[19]
Charge transfer coefficients, cathode	$\alpha_{CAT,\ ANO}$; $\alpha_{CAT,\ CAT}$	1.5; 0.5		[20]

pore former. The composite cathode layers were approximately 40μ thick after firing at 1200 °C. Porous current collecting LSM layers were screen printed on top of the composite layers to improve current collection. The test was performed at 850 °C in air. The spectrum was taken using a Solartron 1260 frequency response analyzer. The test was repeated using different air flow rates with similar results, revealing the absence of mass transport limitations, as expected at open circuit conditions for cells with adequate porosity.

Fitting the model to such an experiment is useful to test the model behaviour upon variation of physical parameters, such as effective conductivities, kinetic constants, and layer thicknesses. The comparison between model and experiment is shown in Fig. 3. The dots correspond to the experimental impedance, and the bold line corresponds to the model result. The model is able to reproduce the experimental data adequately, using only two fitting parameters: the volumetric exchange current to fit the arc size, and the double layer capacitance to fit the peak frequency. However, it is apparent that the experimental impedance arc appears flattened with respect to the numerical impedance. This behaviour could be reproduced using the model (thin line in Fig. 3) by assigning a constant phase element behaviour to the capacitive term in the AC equations. This modification implies changing the $j\omega C$ term in Eq. (22) to $(j\omega C)^{\gamma}$ where γ is a new fitting parameter (0.88 in the present case). This modification does not improve the predictive capabilities of the model, with respect to the changes in impedance behaviour resulting from delamination, however. The new parameter does not have a clear physical meaning, but rather is a mathematical tool to represent, for example, the effect of spatially varying microstructural properties, or of the fractal nature of the interfaces. Nevertheless, the correspondence between the experimental and numerically calculated impedance arcs indicates that the model can reproduce the behaviour of the electrode-electrolyte-electrode system at OCV, using only two fitting parameters.

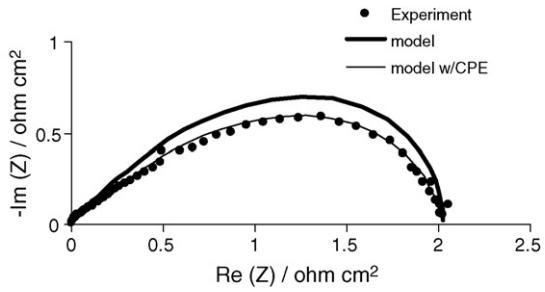

Fig. 3. Fitting of the model to a simplified experiment. The dots correspond to a symmetric cathode test at 850C, around OCV in air. The bold line is the result of the model fitting using only two fitting parameters. The thin line shows the model result if the capacitive behaviour of the electrodes is represented by a constant phase element as opposed to a simple capacitor.

2.6. Delamination

An objective of the present work is to determine under what conditions the presence of a delamination could be detected in the impedance spectrum of a full working solid oxide fuel cell. The impedance of a fuel cell contains information on both the electrochemical processes and the material properties in the cell. Material properties that influence the impedance of a solid oxide fuel cell include bulk and grain boundary conductivities and permittivities. In terms of impedance behaviour, the conductivity is associated with a resistive behaviour, indicating how easily charge carriers travel under the influence of an electric field. The permittivity, on the other hand, is associated with the material's ability to become polarized. In terms of impedance behaviour, the permittivity provides the material with capacitance, that is, a means to store electrical energy. In purely geometrical terms, a delamination is an air filled gap between two adjacent layers of a fuel cell, in a plane that is perpendicular to the main electric current direction. This delamination gap is electrically analogous to a capacitor: filled with air or other gases, it is blocking to direct current, but becomes a conductor of displacement current, in particular alternating current, especially at high frequencies. The capacitance per unit area of this newly formed capacitor is determined by the permittivity of air and the thickness of the discontinuity. Such a feature can be modeled as part of the cell, with the aforementioned electrical characteristics.

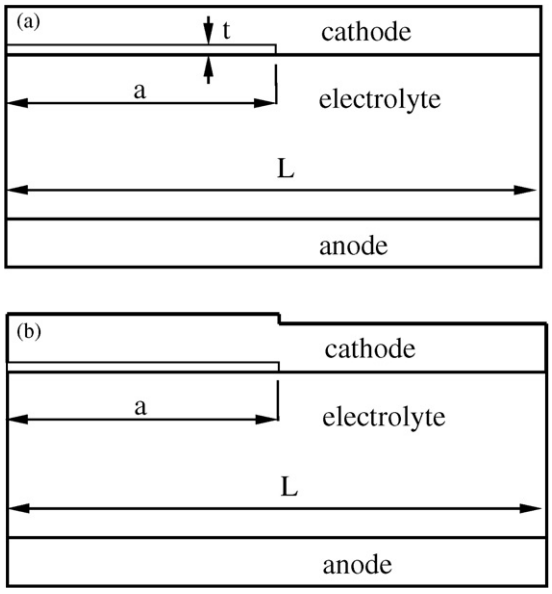

Fig. 4. (a): Schematic view of a delaminated cathode (not to scale). (b): More physically realistic situation corresponding to (a).

In the model, a delamination of the electrode is simulated by an array of elements with the dielectric properties of air inserted between an electrode and the electrolyte, as illustrated in Fig. 4a. In strict physical terms, a delamination implies a detachment of the electrode from the electrolyte (Fig. 4b). However, the simplified geometry shown in Fig. 4a, much easier to handle in the numerical simulations, gave identical results in simulations run with both geometries for comparison purposes, because of the large thickness difference between the delamination and the electrodes. Therefore, the simplified geometry of Fig. 4a was used for subsequent simulations. In the axisymmetric case, the indicated lengths correspond to radii of a circular cell.

The perturbation of the current path introduced by the delamination creates additional requirements that must be considered in the meshing procedure. Meshing geometries that have large aspect ratios require elements of high aspect ratio also, to lower the computational cost. This requirement rules out the possibility of using automated non-structured meshing procedures. Instead, it was necessary to use large aspect ratio rectangular elements as opposed to the standard 2-D triangular elements. As will become clear later, electrochemical activity is negligible in the areas of the electrodes directly above and below the delamination. This is because the large aspect ratio of the cell prevents ions from traveling over long in-plane distances compared to the thickness of the layers being traversed. As a consequence, there is a region of abrupt change in direction and magnitude of the current density around the tip the delamination. If the mesh density here is not adequate, the code routine will not converge. Based on this requirement, the finite element mesh was refined around the delamination tip so that the rapidly varying magnitude of the solved variables was accurately resolved. To facilitate comparisons with future experimental studies using button cells, the axisymmetric geometry is used for the simulation studies presented here.

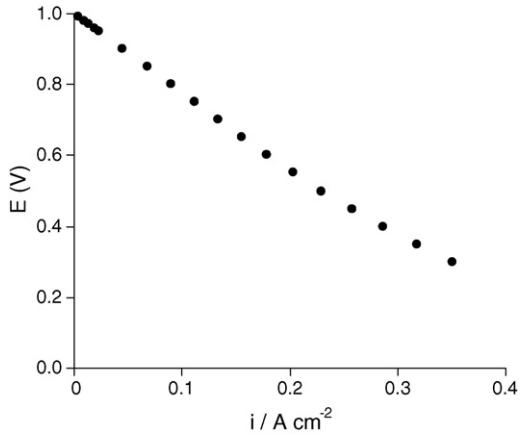

Fig. 5. Polarization curve corresponding to the simulated cell.

3. Model results and discussion

3.1. Intact cell

A polarization curve of the simulated cell is very linear, which is the expected behaviour of an electrolyte-supported cell. Fig. 5 shows the polarization curve. The slope at the 0.7 V operating point is $-2.26\,\text{ohm}\,\text{cm}^2$.

A typical Nyquist impedance plot of an intact cell resulting from this model can be seen in Fig. 6. The diameter of the arcs depends on the reaction rate of the corresponding processes: the faster the processes, the smaller the diameter. In this model, the exchange current density and the charge transfer coefficient determine the rate of the electrochemical reaction. It is important to note that the exchange current densities always appear in the model multiplied by the reaction surface area: $S\,i_0$. We refer to this product as *volumetric* exchange current density. An identical statement applies to the double layer capacitance C_{dl}.

The frequencies studied range from 0.1 Hz to 1 MHz, increasing counterclockwise around the Nyquist plot arcs, logarithmically spaced. The high and low frequency arcs correspond to the anodic and cathodic reactions, respectively. The semicircular shape of the spectrum reflects the capacitive behaviour of the double layer at the electrode/electrolyte interfaces. The linear portion at high frequencies is typical of porous electrodes, where the reaction sites extend beyond the electrode/electrolyte boundary interface into the electrode volume. The Faradaic reaction rate tapers down away from the interface with the electrolyte, and becomes small near the current collector for sufficiently

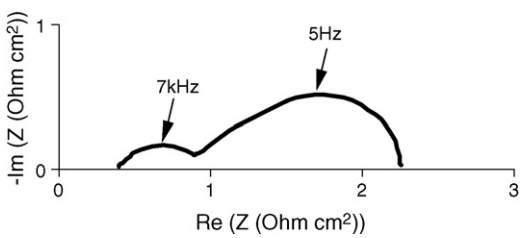

Fig. 6. Impedance spectrum of a unit cell. The linear portion at high frequencies is typical of 3-D composite electrodes, where the reaction extends over the electrode volume.

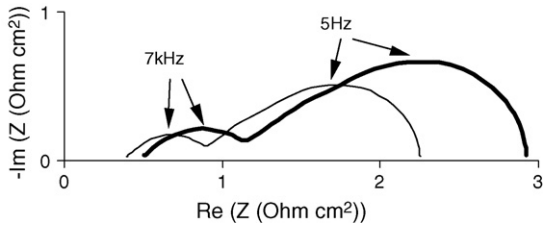

Fig. 7. Bold line: impedance spectrum of an SOFC with a 25% delaminated cathode area. Thin line: impedance spectrum of an equivalent intact cell (Fig. 6). Both series and polarization resistances increase in proportion to the delaminated area, and both electrode semicircle peak frequencies remain unchanged.

thick electrodes, in agreement with the transmission line model [21,22]. That model describes the electrode as a network of resistors and capacitors that represent the ionic and electronic resistance, the double layer capacitance, and the Faradaic resistance. The high frequency intercept corresponds to the Ohmic resistance of the electrolyte.

The impedance plot in Fig. 6 forms the baseline for subsequent parametric studies. The low-frequency intercept corresponds to the total resistance of the cell, and is the sum of the series resistance (high frequency intercept) and the electrode polarization resistances (arc diameters). The spectrum in Fig. 6 intercepts the real axis at 2.25 ohm cm^2, the total resistance of the cell at the operating point. The size of the semicircles is determined by the kinetics of the reactions taking place at both electrodes, as well as by other physical parameters that influence the rate of these reactions, such as ionic conductivity of the electrodes, and the specific active surface areas. These semicircles are referred to as the *electrode semicircles*.

3.2. Delaminated cell

Let L be the radius of a circular cell, a the radius of a delamination in the centre of the cell, t its thickness, and k_{DELAM} its (complex) conductivity. An array of "air" elements inserted between the cathode and the electrolyte with $a/L = 0.5$ (which implies that 25% of the original electrode area is delaminated), $t = 0.2\,\mu$m (see Fig. 4b), $k_{DELAM} = j\omega\varepsilon_0$, and insulation (Neumann) boundary conditions prescribed on all surfaces of the delamination, result in the impedance spectrum shown in Fig. 7.

Two changes are apparent when comparing the impedance spectra of the delaminated and intact cells: (1) the entire plot shifts to the right by approximately 0.11 ohm cm^2, and (2) both electrode arcs increase in diameter, by an amount that is approximately proportional to the delaminated area. The first phenomenon indicates an increase in series resistance due to the reduction of ionic conduction area caused by the delamination. In fact, the new high-frequency intercept is 0.5 ohm cm^2, 29% higher than the corresponding intact cell intercept. The second phenomenon is related to the reduction of available reaction sites caused by the "shadowing" effect of the delamination on the electrodes. As was mentioned earlier, the high aspect ratio of the cell makes in-plane ionic conduction negligible, resulting in the effective non-utilization of the electrode areas above and below the delamination.

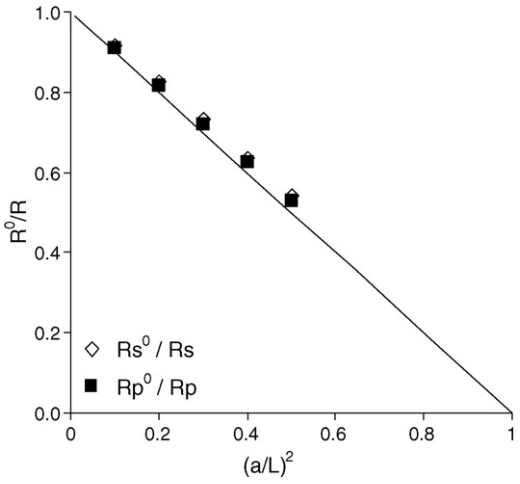

Fig. 8. Normalized polarization resistance and normalized series resistance as a function of the fraction of delaminated electrode area. The line $1-(a/L)^2$ is plotted for comparison. Both polarization and series resistances scale with the extent of delaminated area.

In Fig. 8, the fractional changes in polarization and series resistance are shown as a function of $(a/L)^2$. The resistance changes are normalized as the ratio of intact to degraded resistance, such that the ratio for the intact cell case corresponds to unity, and that for a completely delaminated cell corresponds to zero. In this way, it is possible to compare both resistances consistently. The abscissa indicates the extent of delaminated area, expressed as a fraction of the original electrode area. Fig. 8 indicates that delamination affects both polarization and series resistance in approximately the same proportion as the delaminated area, due to destruction of reaction sites and of conduction area, respectively. The $1-(a/L)^2$ line represents the limiting case of complete shadowing, i.e. total destruction of conductive area or of electrochemically active sites within the electrode. Values larger than those along this line indicate that the shadowing is not total. In the present case, the small extent of lateral ionic conduction in the electrolyte is believed to alleviate the shadowing. Simulations with other cell geometries indicated that the extent of shadowing is larger for thin electrolytes, such as the 10 μ thick electrolytes typically used in anode-supported cells. Simulations performed using Cartesian coordinates yielded equivalent results. The normalized resistances scale, in this case, with a/L, since the 2D approximation corresponds to the rectangular geometry per unit depth. The values for the normalized resistances are also essentially the same for a fixed amount of delaminated area if the delamination consists of a concentric ring from the outer perimeter inward.

In the previous section, it was mentioned that the air gap created by the delamination is expected to show a capacitive effect. However, the extremely low capacitance of this gap makes this capacitive behaviour visible as an extra arc only at very high frequencies. In most cases, these frequencies are beyond the experimental capabilities of state of the art equipment at temperatures of relevance for SOFC's, especially due to lead inductance. Fig. 9 shows the theoretical impedance spectrum extended in frequency to illustrate this point. For higher frequencies, the delamination becomes conductive of displacement

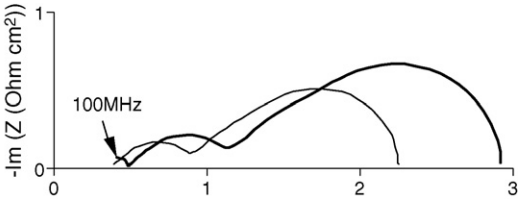

Fig. 9. Solid line: frequency-extended theoretical impedance spectrum showing the high frequency capacitive effect of the delamination gap. Thin line: Impedance spectrum of an equivalent intact cell (Fig. 6).

current, ultimately shorting the delamination gap so that the high frequency intercept is, again, approximately 0.39 ohm cm^2 as it was in the intact cell shown in Fig. 6. The capacitive behaviour shown by the delamination manifests itself as a new semicircle in the Nyquist plot. Crack-induced semicircles in impedance spectra have been reported in the literature for structural ceramics [6–11], where temperatures much lower than typical SOFC operating temperatures made the new feature detectable at frequencies that are readily achievable using state of the art equipment.

Thus, an increase in polarization resistance, when accompanied by the same proportional increase in series resistance with no corresponding change in peak frequency, is a characteristic of a delaminated single solid oxide fuel cell that can be utilized to distinguish that mode of cell degradation from others causing a loss in surface area.

3.3. Parametric studies

It is a goal of the present work to explore the windows of detectability of incipient delamination in an operating SOFC and the applicability of the model to fuel cells with a range of properties. With this purpose, parametric studies were conducted that compare the impedance spectra of the fuel cell for different values of relevant parameters varying over the ranges of interest. The varied parameters include extent of delamination area, DC operating point, and electrode kinetic parameters. The baseline delaminated case corresponds to the conditions that produce the impedance plot shown by the bold line in Fig. 7,

$$\begin{aligned} &(a/L)^2 = 0.25 \\ &t = 0.2\,\mu\text{m} \\ &t_{\text{ELY}} = 150\,\mu\text{m} \\ &S_{\text{CAT}} i_{0,\text{CAT}} = S_{\text{ANO}} i_{0,\text{ANO}} = 2.2 \cdot 10^7 \text{Am}^{-3} \end{aligned} \tag{29}$$

3.3.1. Influence of the extent of delaminated area

It is expected that a change in the delamination length will produce a change in the impedance spectrum of the cell. Fig. 10 illustrates this dependence for $(a/L)^2 = 0.1$, 0.25, and 0.5. The point corresponding to the high frequency intercept in the intact cell shifts to the right with increasing delamination length, corresponding to the increased ohmic drop caused by the reduced available conductive area. This behaviour has been observed experimentally by Hagen et al. [4]. The electrode arcs also show an increase in diameter (polarization resistance) with increasing delamination length, because of the reduction in the number of

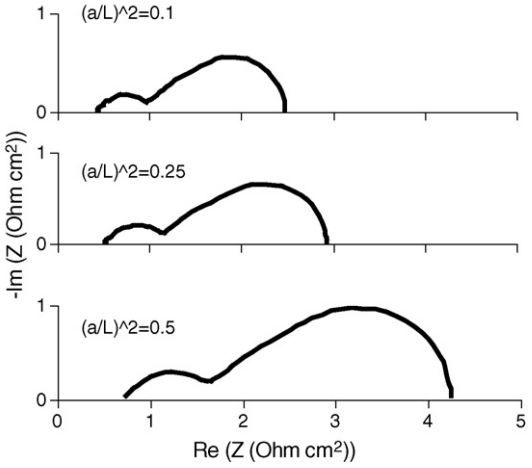

Fig. 10. Influence of the length of the delamination on the impedance, for different values of *a/L*.

active sites caused by the delamination. Since the proportional change in impedance varies with the fraction of delaminated electrode area, the detectability of incipient degradation will to some extent be determined by the initial impedance of the cells, with lower-performing cells experiencing a larger magnitude of change to their initial impedance upon the occurrence of a delamination.

3.3.2. Influence of the electrode kinetics

3.3.2.1. Volumetric exchange current. Different materials and processing routes can yield very different electrochemical kinetics of SOFCs. Therefore, it is useful to study the applicability of the model to cells with different electrode kinetics, particularly regarding the difference in detectability of incipient degradation resulting from different initial values of cell kinetics. Fig. 11 shows the influence of $S\,i_0$ of both electrodes on the impedance behaviour of a delaminated cell. The values for $S\,i_0$ are varied from half the baseline to three times the baseline value. The polarization resistance increases as $S\,i_0$ decreases, while the

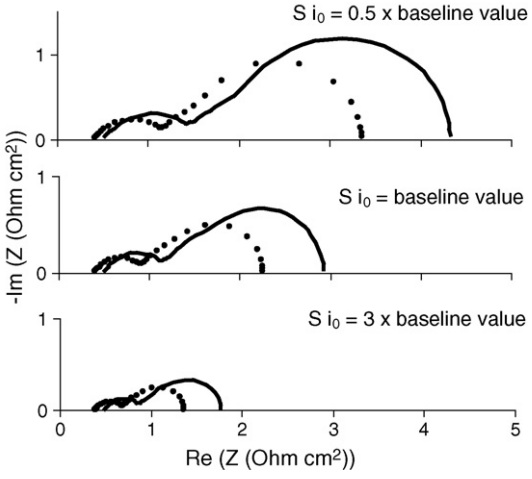

Fig. 11. Influence of the electrode kinetics on the impedance spectra. Part I: volumetric exchange current. Dots: intact cell. Lines: delaminated cell.

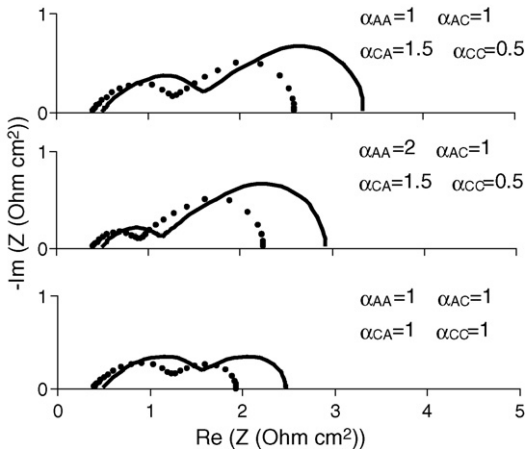

Fig. 12. Influence of the electrode kinetics on the impedance spectra. Part 2: charge transfer coefficients. Dots: intact cell. Lines: delaminated cell.

series resistance remains constant. Therefore, neither variability of cell properties nor uncertainty in the knowledge of cell kinetic parameters are expected to adversely affect the applicability of the model to detecting changes in impedance caused by delamination. However, cells with higher initial performance will experience changes in impedance that are harder to resolve upon the first appearance of an incipient delamination.

3.3.2.2. Charge transfer coefficients. Changes in the charge transfer coefficients yield analogous results to those described above. Despite the considerable uncertainty encountered in the literature regarding the values of the charge transfer coefficients, their magnitude is of the order of unity. The reason is that the charge transfer coefficient for a given electrode reaction (and a given direction, anodic or cathodic) results from the product of a symmetry coefficient times the number of electrons transferred during the charge transfer portion of the total electrode reaction. The symmetry coefficient ranges from zero to one, and it is often assumed equal to 0.5. This quantity is a measure of the bias of the energy barrier that needs to be overcome for an electrode reaction to happen. Regardless of the electrode reaction under consideration, the number of electrons transferred in the rate-limiting reaction step seldom exceeds four. For these reasons, the charge transfer coefficients typically range from 0.5 to 2. An exact knowledge of the charge transfer coefficients is, however, not necessary for the conclusions resulting from the model of changes in cell behaviour due to delamination to be valid. Fig. 12 shows the trends in impedance spectra for both the intact and delaminated cathode cases for three different values of charge transfer coefficients. The same proportional changes to the series and polarization resistances are observed for all three of the cases, suggesting that the changes caused by delamination are independent of cell kinetics, with only the resolution of detectability being potentially affected by the values of the cell kinetic parameters.

3.3.3. Operating point

The ability of this model to reproduce the experimental data presented in Section 2.5 is restricted to an operating point close

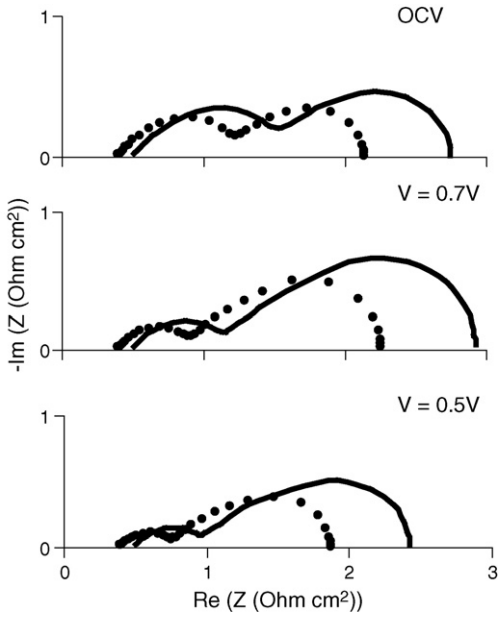

Fig. 13. Influence of the operating point on the impedance spectra. Dots: intact cell. Lines: delaminated cell.

to equilibrium. This is, of course, not a practical operating point since no power is generated. A parametric study of the impedance behaviour upon delamination as a function of DC bias indicates that the impedance trend is consistent with the results reported so far, as shown in Fig. 13. Polarization of the cell away from open circuit conditions causes a reduction of the electrode arc diameter, to an extent that is related to the magnitude of the charge transfer coefficient in the relevant direction of each electrode, namely the charge transfer coefficient in the cathodic reaction direction for the cathode and the charge transfer coefficient in the anodic reaction direction for the anode.

In all cases, both polarization and series resistances change proportionally to the extent of the delaminated area. As far as the applicability of this method for detecting delamination is concerned, the simulations show that the presence of electrode delamination produces consistent effects, regardless of the kinetic parameters of the cells. It is the nature of the changes in impedance that provides evidence of delamination, rather than the value of the impedance itself.

Table 2 summarizes the results of the parametric studies described above. Completely consistent changes in both series and polarization resistances would imply, in theory, that all values of Rp^0/Rp (third column) should be identical for cases 2, 3, and 4. The reason for the slight differences observed in the model predictions is that the series resistance is calculated as the real impedance at 1 MHz, corresponding to a practical upper limit for experimental measurements in the presence of inductance. From the experimental standpoint, this frequency is high enough for typical SOFC operating temperatures. However, there are small differences (∼1%) in the values of the real impedance at 1 MHz for the different parameterizations. Extrapolations to very high frequencies with the model yielded the theoretically expected values.

Table 2
Summary of normalized changes in series and polarization resistances for different parametric studies

	Rs°/Rs	Rp°/Rp
Intact cell	1	1
Baseline delamination	**0.777**	**0.769**
1. Extent of delaminated area $(a/L)^2$		
0	1	1
0.1	0.916	0.910
0.25	**0.777**	**0.769**
0.5	0.542	0.529
2. Volumetric exchange current density $S\,i_0/(S\,i_0)_{\text{baseline}}$		
0.5	0.777	0.773
1	**0.777**	**0.769**
3	0.777	0.764
3. Charge transfer coefficients [α_{AA} α_{AC} α_{CA} α_{CC}]		
[2.0 1.0 1.5 0.5]	**0.777**	**0.769**
[1.0 1.0 1.5 0.5]	0.777	0.776
[1.0 1.0 1.0 1.0]	0.777	0.785
4. Operating point Vcell (V)		
OCV	0.777	0.780
0.7	**0.777**	**0.769**
0.5	0.777	0.768

The baseline delamination case (Eq. (29)) is highlighted in bold. The effect of delamination is the same over the range of parameters studied.

4. Conclusions

Electrode delamination in a single solid oxide fuel cell degrades the cell performance by reducing the available species conduction area, and by rendering electrochemically inactive the electrode reaction surface area above and below the delamination. A finite element model of an operating solid oxide fuel cell shows that the presence of delamination can be detected using electrochemical impedance spectroscopy. This degradation mechanism causes a simultaneous and equivalent increase in the series and polarization resistance of the cell. The series and polarization resistances both increase proportionally to the delaminated area. The normalized changes in series and polarization resistances are introduced as a useful means to compare the extents of degradation caused by different degradation mechanisms.

The trend found for series and polarization resistance changes upon delamination is independent of the fuel cell kinetic parameters and of the operating point within the ranges examined. Therefore, the predicted trends in the results are applicable to cells of a wide range of materials and made with different processing methods.

A new time constant also appears in the impedance spectrum of a delaminated solid oxide fuel cell due to the capacitive effect of the material discontinuity. However, the capacitive behaviour of the delamination gap is not observable within experimentally achievable frequency ranges at typical operating temperatures of an SOFC. The relatively high electrolyte conductivity, combined with the very low permittivity of the air filling the delamination gap, result in a relaxation frequency beyond the experimental capabilities of state of the art equipment.

Acknowledgements

The authors gratefully acknowledge financial support from the Natural Sciences and Engineering Research Council of Canada, and use of fuel cell testing facilities at the National Research Council of Canada.

References

[1] S. Singhal, K. Kendall (Eds.), High-Temperature Solid Oxide Fuel Cells: Fundamentals, Design and Applications, Elsevier, Oxford, 2003, p. 73.
[2] E. Ivers-Tiffée, Q. Weber, D. Herbstritt, J. Eur. Ceram. Soc. 21 (2001) 1805–1811.
[3] R. Barfod, M. Mogensen, T. Klemensoe, A. Hagen, Y. Liu, Proc. SOFC IX 1 (2005) 524–533.
[4] A. Hagen, R. Barfod, P. Hendriksen, Y. Liu, Proc. SOFC IX 1 (2005) 503–513.
[5] S. Xia, V. Birss, Proc. SOFC IX 2 (2005) 1275–1283.
[6] L. Dessemond, M. Kleitz, J. Eur. Ceram. Soc. 9 (1992) 35–39.
[7] M. Kleitz, C. Pescher, L. Dessemond, Sci. Technol. Zirconia 5 (1993) 593–608.
[8] A. Tiefenbach, Electrische Charakterisierung mechanischer Schaedigungen in ZrO2-Keramik, VDI:-Fortschrittsberichte 5/555, VDI-Verlag, Duesseldorf, 1999.
[9] A. Tienfenbach, B. Hoffmann, J. Eur. Ceram. Soc. 20 (2000) 2079–2094.
[10] A. Tienfenbach, S. Wagner, R. Oberacker, B. Hoffmann, Ceram. Int. 26 (2000) 745–751.
[11] J. Fleig, J. Maier, Solid State Ionics 85 (1996) 17–24.
[12] J. Newman, C. Tobias, J. Electrochem. Soc. 109 (12) (1962) 1183–1191.
[13] J. Deseure, Y. Bultel, L. Dessemond, E. Siebert, Electrochim. Acta 50 (2005) 2037–2046.
[14] R. Williford, L. Chick, G. Maupin, S. Simner, J. Stevenson, J. Electrochem. Soc. 8 (150) (2003) A1067–A1072.
[15] S. Primdahl, M. Mogensen, J. Appl. Electrochem. 30 (2000) 247–257.
[16] M. Juhl, S. Primdahl, C. Manon, M. Mogensen, J. Power Sources 61 (1996) 173–181.
[17] M. Jørgensen, S. Primdahl, M. Mogensen, Electrochim. Acta 44 (1999) 4195–4201.
[18] M. Jørgensen, M. Mogensen, J. Electrochem. Soc. 148 (5) (2001) A433–A442.
[19] T. Kawada, N. Sakai, H. Yokokawa, M. Dokiya, J. Electrochem. Soc. 137 (10) (1990) 3042–3047.
[20] B. Kenney, K. Karan, Proceedings of Hydrogen and Fuel Cells 2004, 2004, pp. 1–11.
[21] R. De Levie, Adv. Electrochem. Electrochem. Eng. 6 (1967) 329.
[22] E. Barsoukov, J. MacDonald (Eds.), Impedance Spectroscopy, 2005, p. 531.